



HAL
open science

MusE GAs FLOW and Wind (MEGAFLOW)

Ilane Schroetter, Nicolas F. Bouché, Johannes Zabl, Martin Wendt, Maxime Cherrey, Ivanna Langan, Joop Schaye, Thierry Contini

► **To cite this version:**

Ilane Schroetter, Nicolas F. Bouché, Johannes Zabl, Martin Wendt, Maxime Cherrey, et al.. MusE GAs FLOW and Wind (MEGAFLOW). *Astronomy and Astrophysics - A&A*, 2024, 687, pp.A39. 10.1051/0004-6361/202348725 . hal-04625104

HAL Id: hal-04625104

<https://hal.science/hal-04625104v1>








Submitted on 25 Jun 2024

HAL is a multi-disciplinary open access archive for the deposit and dissemination of scientific research documents, whether they are published or not. The documents may come from teaching and research institutions in France or abroad, or from public or private research centers.

L'archive ouverte pluridisciplinaire **HAL**, est destinée au dépôt et à la diffusion de documents scientifiques de niveau recherche, publiés ou non, émanant des établissements d'enseignement et de recherche français ou étrangers, des laboratoires publics ou privés.

MusE GAs FLOW and Wind (MEGAFLOW)

XI. Scaling relations between outflows and host galaxy properties[★]

Ilane Schroetter¹, Nicolas F. Bouché², Johannes Zabl^{2,6}, Martin Wendt³, Maxime Cherrey²,
Ivanna Langan^{4,2}, Joop Schaye⁵, and Thierry Contini¹

¹ Institut de Recherche en Astrophysique et Planétologie, Université de Toulouse, CNRS, CNES, UPS, 9 Av. du colonel Roche, 31028 Toulouse Cedex 04, France

e-mail: ilane.schroetter@gmail.com

² Centre de Recherche Astrophysique de Lyon (CRAL) UMR5574, Univ Lyon1, Ens de Lyon, CNRS, 69230 Saint-Genis-Laval, France

³ Institut für Physik und Astronomie, Universität Potsdam, Karl-Liebknecht-Str. 24/25, 14476 Golm, Germany

⁴ European Southern Observatory, Karl-Schwarzschild-Str. 2, 85748 Garching, Germany

⁵ Leiden Observatory, Leiden University, PO Box 9513, 2300 RA Leiden, The Netherlands

⁶ Institute for Computational Astrophysics and Department of Astronomy & Physics, Saint Mary's University, 923 Robie Street Halifax, Nova Scotia B3H 3C3, Canada

Received 24 November 2023 / Accepted 4 April 2024

ABSTRACT

Absorption line spectroscopy using background quasars can provide strong constraints on galactic outflows. In this paper we investigate possible scaling relations between outflow properties, namely outflow velocity V_{out} , mass ejection rate \dot{M}_{out} , and mass loading factor η , and the host galaxy properties, such as star formation rate (SFR), SFR surface density, redshift, and stellar mass, using galactic outflows probed by background quasars from MEGAFLOW and other surveys. We find that $V_{\text{out}}(\eta)$ is (anti-)correlated with SFR and SFR surface density. We extend the formalism of momentum-driven outflows from a previous study to show that it applies not only to “down-the-barrel” studies, but also to winds probed by background quasars, suggesting a possible universal wind formalism. Under this formalism, we find a clear distinction between strong and weak outflows where strong outflows seem to have tighter correlations with galaxy properties (SFR or galaxy stellar mass) than weak outflows.

Key words. galaxies: evolution – galaxies: formation – intergalactic medium – galaxies: kinematics and dynamics – quasars: absorption lines

1. Introduction

In the era of modern cosmology with well-determined cosmological parameters, the process (or processes) responsible for the low efficiency of galaxy formation is still unknown. The efficiency of galaxy formation, defined as the fraction of baryons in galaxies relative to the amount of baryons available for a given cosmology, is low, ranging from a few percent to 20% (e.g., Behroozi et al. 2013; Moster et al. 2013). The peak occurs at around the Milky Way dark matter mass (or $10^{12} M_{\odot}$). At low masses, it is common to invoke feedback processes such as supernovae explosions (e.g., Dekel & Silk 1986), radiation pressure (e.g., Murray et al. 2005; Hopkins et al. 2012), cosmic rays, or stellar winds to account for the low efficiency of galaxy formation. At higher masses, feedback processes from active galactic nuclei (AGN) are thought to play a major role (e.g., Silk & Rees 1998). Both SN-driven and AGN-driven outflows would drive baryons out of galaxies back into the circumgalactic medium (CGM).

The CGM, loosely defined as the region surrounding galaxies (within the virial radius, or <100–150 kpc), is where the

signatures of these complex feedback processes for galaxy evolution are to be found, including gas accretion of the intergalactic medium (IGM). Thus, observations of the CGM are crucial in order to put constraints on galaxy formation numerical models. However, the CGM is difficult to observe directly because the gas density is orders of magnitude lower than the interstellar medium of the host galaxy. Fortunately, bright background sources like quasars are effective probes to study the CGM because they are sensitive to low gas (or column) densities around foreground objects and they also reveal the presence of the kinematics of gaseous halos around any type of galaxy, irrespective of their luminosity or star formation rate (SFR; e.g., Bouché et al. 2007, 2012; Turner et al. 2014; Kacprzak et al. 2014; Schroetter et al. 2015, 2016; Muzahid et al. 2015; Rahmani et al. 2018; Mary et al. 2020).

Compared to traditional techniques requiring imaging and expensive spectroscopic campaigns (e.g., Bergeron & Stasinska 1986; Steidel et al. 1995; Nielsen et al. 2013), integral field units (IFUs) combined with background quasars provide the most efficient way to study the properties of gaseous halos surrounding galaxies because they simultaneously yield the redshifts of all galaxies in the field of view, thereby allowing for a rapid identification of absorption-galaxy pairs (e.g., Bouché et al. 2012; Schroetter et al. 2015, 2016, 2019; Zabl et al. 2019; Martin et al.

[★] Based on observations made at the ESO telescopes at La Silla Paranal Observatory under program IDs 094.A-0211(B), 095.A-0365(A), 096.A-0164(A), 097.A-0138(A), 099.A-0059(A), 096.A-0609(A), 097.A-0144(A), 098.A-0310(A), 293.A-5038(A).

2019; Muzahid et al. 2020). Wide-field IFUs, for example MUSE (Bacon et al. 2006, 2010, 2015), are especially important given that they can study absorption-galaxy pairs up to 200–300 kpc, going beyond a typical virial radius at intermediate redshifts.

In the past years, several IFU surveys have yielded large samples of absorption-galaxy pairs, such as MUSEQuBES (Muzahid et al. 2020), CUBS (Chen et al. 2020), and MAGG (Lofthouse et al. 2020). In particular, our MUSE GAs FLOW and Wind survey (MEGAFLOW) has yielded a sample of more than 100 Mg II absorber-galaxy pairs at $0.4 < z < 1.5$ (Bouché et al., in prep.). A clear result from this survey and others (e.g., Bordoloi et al. 2011; Bouché et al. 2012; Kacprzak et al. 2011; Schroetter et al. 2015; Ho et al. 2017; Lan & Fukugita 2017; Lundgren et al. 2021) is that the cool CGM is anisotropic with an excess Mg II absorption along the minor and major axes of star-forming galaxies (SFGs), indicating two physical mechanisms responsible for the Mg II absorption around galaxies, the former being outflows (Schroetter et al. 2016, 2019) and the latter being extended gaseous disks (Zabl et al. 2019). This dichotomy is supported by the absorption kinematics with respect to the host (Schroetter et al. 2019; Zabl et al. 2019; see also Kacprzak et al. 2011; Nielsen et al. 2015; Bordoloi et al. 2011; Martin et al. 2019; Lundgren et al. 2021), and allows one to study the properties of outflows (e.g., kinematics, mass outflow rates).

While numerous studies exist on galactic outflows using traditional spectroscopy (called the “down-the-barrel” technique) (e.g., Genzel et al. 2011; Martin 2005; Heckman et al. 2015), only a few groups have used the background quasar (QSO) technique to put constraints on outflow properties (e.g., outflow velocity): the KBSS survey (Steidel et al. 2014), a galaxy redshift survey around 15 luminous QSOs; the COS-burst survey (Heckman et al. 2017) around 17 low-redshift starburst galaxies; the Keck survey for Mg II halos around 50 $z \sim 0.2$ normal SFGs (Martin et al. 2019).

In this paper we focus on the properties (outflow velocity, ejected mass rate, and mass loading factor) of galactic outflows and investigate possible scaling relations with the properties of the host galaxy. The paper is organized as follows. In Sect. 2 we briefly present the MEGAFLOW sample. In Sect. 3 we investigate the different wind properties and compare them with the host galaxy properties, adding other studies in search of possible scaling relations. In Sect. 4 we discuss the possible origin of outflow mechanisms. In Sect. 5 we present the discussion and our conclusions.

Throughout the paper we use a 737 cosmology ($H_0 = 70 \text{ km s}^{-1} \text{ Mpc}^{-1}$, $\Omega_m = 0.3$, and $\Omega_\Lambda = 0.7$) and a Chabrier (2003) stellar initial mass function (IMF).

2. Data

2.1. The MEGAFLOW survey

The MusE GAs FLOW and Wind (MEGAFLOW) survey consists of 22 quasar fields selected to have multiple strong Mg II absorption lines (rest-frame equivalent width $W_r^{12796} > 0.5\text{--}0.8 \text{ \AA}$) in the Zhu & Ménard (2013) catalog based on the Sloan Digital Sky Survey (SDSS; Ross et al. 2012; Alam et al. 2015), which resulted in 79 strong Mg II absorbers¹. The survey was designed to study the properties of gas flows surrounding SFGs detected using the Multi-Unit Spectroscopic Explorer

¹ 79 absorbers in DR1 of MEGAFLOW, with now up to 127, which constitutes DR2.

(MUSE, Bacon et al. 2010) on the Very Large Telescope (VLT). For each quasar we carried out high-resolution spectroscopic follow-up observations with the Ultraviolet and Visual Echelle Spectrograph (UVES, Dekker et al. 2000).

We refer to Schroetter et al. (2016, hereafter Paper I) for a more detailed understanding of the observational strategy, and to Zabl et al. (2019, hereafter Paper II) for data reduction. In Schroetter et al. (2019, hereafter Paper III), we constrained outflow properties of 27 $z \approx 1$ host galaxies; specifically, we constrained the outflow velocity V_{out} , the mass outflow rate \dot{M}_{out} and the mass loading factor $\eta = \dot{M}_{\text{out}}/\text{SFR}$ (i.e., the ratio of the mass ejected rate to the SFR). In this paper we address whether these outflow properties follow scaling relations with host galaxy properties (e.g., SFR, stellar mass (M_*), redshift).

2.2. Previous studies on galactic winds

In order to augment the results of Paper III with other outflow studies that also used the background quasar technique, here we include (Bouché et al. 2012, hereafter B12), who used a catalog of 11 galaxy-quasar pairs² from a combination of SDSS, Keck LRIS, and OTA observations; the four wind cases in the SIMPLE sample (Schroetter et al. 2015), which are a combination of VLT/SINFONI and UVES observations; Heckman et al. (2017, hereafter H17), who built the COS-burst catalog containing 17 starburst galaxies selected from the SDSS data release 7 (DR7) and QSOs from the GALEX DR6 catalog; and Martin et al. (2019, hereafter M19), who used a sample of 50³ galaxy-quasar pairs at $z \approx 0.2$.

To compare wind properties from background quasars to the more common down-the-barrel technique, we also used Heckman et al. (2015, hereafter H15), who used the COS-FUSE and the COS-LBA surveys (Grimes et al. 2009; Alexandroff et al. 2015, respectively), and Perrotta et al. (2023, hereafter P23), who used a sample of 14 starbursts based on the SDSS DR8 catalog. Table 1 summarizes the characteristics of these surveys. As there are many down-the-barrel studies, we chose only those that reported outflow properties, for example the ejected mass outflow rates and mass loading factor. The two down-the-barrel studies H15 and P23 were chosen for the following reasons: they focus on low-redshift galaxies ($z < 0.8$) and are thus complementary to our $z \approx 1$ sample; the stellar mass range probed is similar to ours ($\log M_*/M_\odot \approx 7\text{--}12$); and the galaxies are starbursting, and are thus complementary to our more normal star-forming galaxies. Table 1 summarizes the general properties of each study. Concerning SFRs of the MEGAFLOW galaxies, Paper III discusses the possible bias between using SED fitting and [O II] emission. Comparing SFRs from different samples, they find that there is no systematic bias between the two methods.

2.3. Sample general properties

To better understand the evolutionary state of the various samples, we show the selected literature galaxy samples and MEGAFLOW+SIMPLE (Schroetter et al. 2015) galaxies relative to the main sequence (MS) between SFR and galaxy stellar mass M_* in Fig. 1. In order to account for the redshift evolution, we chose to use the relation derived by Boogaard et al. (2018) and normalized for a redshift $z = 0.2$. In this figure we clearly

² Five of these pairs are in a configuration for wind studies.

³ Thirty of these galaxies have Mg II velocities, of which only 16 have an azimuthal angle with their quasar suitable for wind studies.

Table 1. Summary of other wind studies.

Paper (1)	N_{gal} (2)	z_{gal} (3)	SFRs (4)	Galaxy type (5)	$\log(M_{\star}/M_{\odot})$ (6)	Method (7)
Paper III	27	$0.5 < z < 1.5$	[O II]	SFGs	8.5–11	Background QSO
B12	5	$z \approx 0.1$	SED	SFGs	10–11	Background QSO
S15	4	$0.5 < z < 1.5$	[O II]	SFGs	8.5–11	Background QSO
H17	17	$z < 0.2$	SED	Starbursts	10–11	Background QSO
M19	16	$z < 0.4$	SED	SFGs	9–11	Background QSO
H15	32	$z < 0.2$	SED	Starbursts	7–11	Down-the-barrel
P23	14	$z \approx 0.5$	SED	Starbursts	10.5–11.2	Down-the-barrel

Notes. (1) Study name, Paper III for Schroetter et al. (2019), B12 for Bouché et al. (2012), S15 for the SIMPLE wind cases in Schroetter et al. (2015), H15 and H17 respectively for Heckman et al. (2015 and 2017), M19 for Martin et al. (2019), and P23 for Perrotta et al. (2023); (2) Sample size in galaxy number. (3) Redshift range; (4) Method used to estimate galaxy SFR; (5) Type of galaxy; (6) Galaxy stellar mass range; (7) Method used to constrain outflow properties.

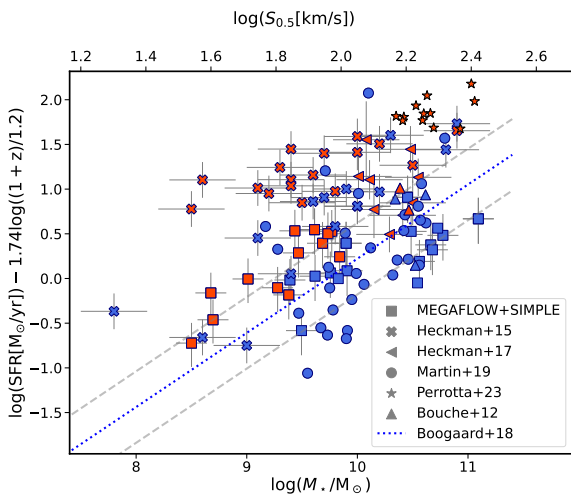


Fig. 1. SFR- M_{\odot} main sequence. The data points are normalized for redshift evolution to $z = 0.2$. All the SFRs are also corrected to have the same initial mass function (a Chabrier 2003 IMF). The Boogaard et al. (2018) MS relation is represented by the dotted blue line along with its intrinsic scatter of 0.4 dex (gray dashed lines). As described in the text (Sect. 3.1), red (blue) galaxies are considered strong (weak) outflow cases.

see that H15 galaxies are in the high SFR part, close to starburst galaxies, whereas the MEGAFLOW and M19 galaxies appear to be mainly located on the MS at $z = 0.2$. In Fig. 1 the red symbols represent either starbursts (for P23 and H17) or strong outflow cases (for H15, M19, and Paper III galaxies), as described in Sect. 3.1.

3. Results

In order to compare wind studies using background quasars to other types of studies, we first need to establish a common framework. In particular, H15 makes a distinction between strong and weak outflows based on the wind momentum compared to the momentum injection rate from SFR, and extend their formalism to winds probed by background quasars sight-lines.

3.1. Wind formalism

Following H15, in the case of momentum-driven winds where the momentum injection rate \dot{p}_{\star} is supplied by the star-forming

or starburst galaxy, the outward force from the momentum injection is countered by gravity. For an outflow to develop, the outward force ought to be greater than gravity, defining a critical momentum injection rate \dot{p}_{crit} (e.g., H15).

For a cloud outflow model (to be consistent with Bouché et al. 2012 and Schroetter et al. 2015), the outward force is the pressure P_w times the cloud area A_c ,

$$F_w = P_w A_c = \frac{\dot{p}_{\star}}{\Omega_w r^2} A_c, \quad (1)$$

where Ω_w is the wind solid angle and r the location of the wind, while the inward gravitational force is

$$F_g = \frac{G M(<r)}{r^2} m_c = \frac{v_{\text{circ}}^2}{r} m_c, \quad (2)$$

where G is the gravitational constant and v_{circ}^2 the galaxy circular velocity. For a cloud of mass m_c and area A_c , the critical momentum flux $\dot{p}_{\text{crit},c}$ is given by $F_w \geq F_g$, or $\dot{p}_{\text{crit},c}(r) A_c \geq \Omega_w v_{\text{circ}}^2 r m_c$, such that, if one writes the cloud mass as $m_c = A_c(r) N_c(r) \langle m \rangle$, where $N_c(r)$ is the cloud column density and $\langle m \rangle$ is the mean mass per particle, the critical momentum flux is

$$\begin{aligned} \dot{p}_{\text{crit},c}(r) &= \Omega_w v_{\text{circ}}^2 r m_c / A_c \\ &= \Omega_w v_{\text{circ}}^2 r N_c(r) \langle m \rangle. \end{aligned} \quad (3)$$

This critical momentum flux required in order to have a net outward force on an outflowing cloud is [H15]

$$\dot{p}_{\text{crit},c}(r) = 10^{33.9} \text{ dyn} \frac{\Omega_w}{4\pi} \frac{N_c(r)}{10^{21} \text{ cm}^{-2}} \frac{r}{1 \text{ kpc}} \left(\frac{v_{\text{circ}}}{100 \text{ km s}^{-1}} \right)^2. \quad (4)$$

In other words, winds will only develop when $\dot{p}_{\star} > \dot{p}_{\text{crit},c}$.

Comparing this critical momentum flux $\dot{p}_{\text{crit},c}$ to the momentum injection rate \dot{p}_{\star} , which is $\dot{p}_{\star} = 4.8 \times 10^{33}$ SFR dynes, one can distinguish between weak and strong outflows. H15 defined weak winds when $0 < \log(\dot{p}_{\star}/\dot{p}_{\text{crit},c}) < 1.0$ and strong winds when $\log(\dot{p}_{\star}/\dot{p}_{\text{crit},c}) > 1.0$. This means that these regimes are the two cases where their momentum flux is higher or lower than ten times the critical momentum flux required to have a net outward force on an outflowing cloud. H15 made this arbitrary limit to where the strong outflow seems to carry a significant amount (on the order of unity) of the momentum flux available from the starburst.

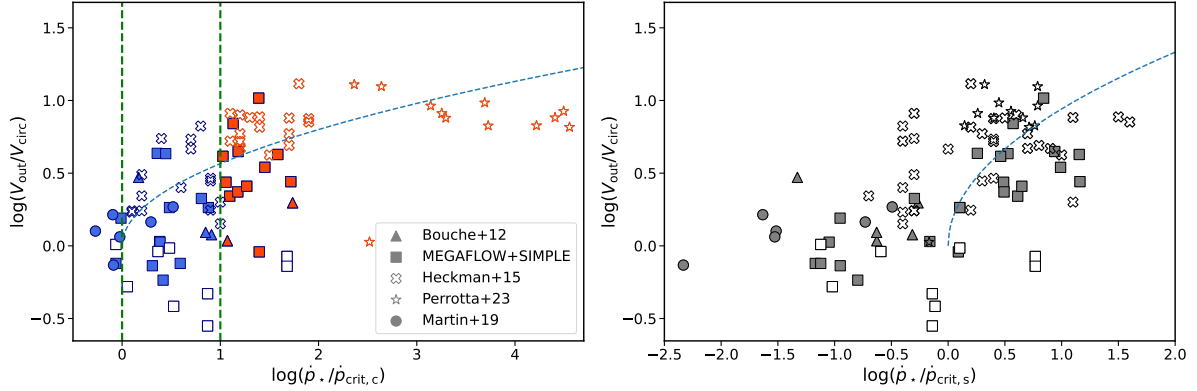


Fig. 2. Normalized outflow velocity ($V_{\text{out}}/V_{\text{circ}}$) as a function of the ratio of the amount of momentum flux supplied by star formation to the value needed to overcome gravity and push the outflowing gas for a cloud model (left) and for a shell model (right). This figure is similar to Fig. 9 in H15. Squares, crosses, triangles, circles, and stars represent respectively the MEGAFLOW, H15, B12, M19, and P23 galaxies. Empty symbols represent down-the-barrel data, whereas filled symbols are from background quasars studies. The left panel, in blue (red), shows the weak (strong) outflows. In the left (right) panel the dashed curve is derived from the equation of motion for a cloud (shell) model (see text). The white squares correspond to less reliable MEGAFLOW outflow properties (for more details, see Schroetter et al. 2019).

From Eqs. (1) and (2), the equation of motion for such a cloud launched from R_0 is (e.g., Murray et al. 2005; Heckman et al. 2015)

$$\frac{1}{2}v^2 = \int_{R_0}^r dr \left(\frac{\dot{p}_*}{\Omega_w r^2 m_c} - \frac{v_{\text{circ}}^2}{r} \right) = v_{\text{circ}}^2 \int_{R_0}^r dr \left(\frac{R_g}{r} - 1 \right) \frac{1}{r}, \quad (5)$$

$$v(r) = \sqrt{2} v_{\text{circ}} \sqrt{\left(1 - \frac{R_0}{r}\right) \frac{R_g}{R_0} - \ln\left(\frac{r}{R_0}\right)}, \quad (6)$$

where $R_g = \dot{p}_*/(\Omega_w v_{\text{circ}}^2 N_c < m >)$ defines the radius at which the velocity peaks at v_{max}

$$\begin{aligned} v_{\text{max}} &= \sqrt{2} v_{\text{circ}} \sqrt{\left(\frac{\dot{p}_*}{\dot{p}_{\text{crit},c}}\right) - 1 - \ln\left(\frac{\dot{p}_*}{\dot{p}_{\text{crit},c}}\right)} \\ &\approx \sqrt{2} v_{\text{circ}} \sqrt{\frac{R_g}{R_0}} \quad \text{can be } \gg \sqrt{2} v_{\text{circ}}, \end{aligned} \quad (7)$$

where $R_g/R_0 = \dot{p}_*/\dot{p}_{\text{crit},c}(R_0)$ (defined as R_{crit} in Heckman et al. 2015).

It should be noted that this formalism makes a number of implicit assumptions. First, it assumes that the potential is that of an isothermal sphere, $v_{\text{circ}}^2 = \frac{GM(<r)}{r} = 2\sigma^2$, which implies that v_{circ} is independent of radius. Second, the expression for the critical momentum injection rate \dot{p}_{crit} is estimated at $r = R_0$, where R_0 is the launch radius. H15 uses $R_0 = r_* = 1$ kpc.

In the case of background sight lines, the critical momentum $\dot{p}_{\text{crit},c}$ is only evaluated at $r = b$, where b is the impact parameter. However, assuming that outflows are mass conserving (i.e., $\rho(r)r^2$ is constant, such that $N(r)r$ is conserved), then Eq. (3) implies that $\dot{p}_{\text{crit},c}$ is independent of radius, $\dot{p}_{\text{crit},c}(b) = \dot{p}_{\text{crit},c}(R_0)$, provided that the circular velocity v_{circ} is roughly constant.

Following H15, we also looked at a shell model for the outflowing gas⁴ using the critical momentum injection $\dot{p}_{\text{crit},s} = f_s v_{\text{circ}}^4 / G$, where the shell mass fraction $f_s \equiv M_s / M(<r)$ is ~ 0.1 . Figure 2 (right) shows that a shell model (Eq. (6) in H15) does not match the data compared to the cloud model shown in the left panel. We thus chose the cloud model as it appears to better describe the data.

⁴ The shell wind model assumes that the outward force p_* is greater than the shell gravity $M_s v_{\text{circ}}^2 / r_s$ for a shell mass M_s at radius r_s .

3.2. A universal formalism

In order to test this formalism, we first compared the outflow velocity to the wind strengths, which is plotted in Fig. 2. This figure shows the normalized outflow velocity $v_{\text{out}}/v_{\text{circ}}$ as a function of $\log(\dot{p}_*/\dot{p}_{\text{crit},c})$ ratio for the MEGAFLOW (Paper III), H15, M19⁵, and P23 galaxies for a cloud and a shell model in the left and right panels, respectively. For the galaxies in Paper III, we used $v_{\text{circ}} \approx S_{0.5} = \sqrt{0.5V_{\text{max}}^2 + \sigma^2}$ where V_{max} is the intrinsic galaxy rotational velocity (corrected for the galaxy inclination), while H15 used the observed rotational velocity. Finally, we used the bi-conical shape of our outflows with a cone opening angle of $2\theta = 60^\circ$ because of the azimuthal bi-modality in Mg II (Bordoloi et al. 2011; Bouché et al. 2012; Schroetter et al. 2015; Lundgren et al. 2021). This led to a downward correction of the H15 estimations of their ejected mass rate⁶. We also used their updated outflow velocities values (Heckman & Borthakur 2016). In addition, we investigated for a possible correlation between sight-line impact parameter and whether the outflow is classified as strong or weak, but found none.

In Fig. 2 and subsequently, we use blue (red) symbols for weak (strong) outflows when showing MEGAFLOW, H15, M19, and P23 results. In addition, throughout the paper the white squares correspond to galaxies in Paper III where the wind model does not fit the spectra convincingly⁷. In addition to differentiating between weak and strong outflows in blue and red, respectively, we also use empty markers for the down-the-barrel cases, namely H15 and P23, throughout the paper for a clear distinction between the two methods.

⁵ For M19 systems we only use those with a REW W_r^{12796} larger than 0.5 \AA in order to match the MEGAFLOW sample selection and have a consistent estimation of the hydrogen column density, which reduces the number of galaxies from 16 to 8 for this sample.

⁶ To get from a spherical to a bi-conical outflow with opening angles of 60° geometry, the reduction is approximately 8.

⁷ The reasons for each case are described in Paper III, one of the main reasons is that the absorption system has multiple components, and thus is too complex to be reproduced by the simple wind model as the absorption most likely is a combination of multiple galaxy contributions.

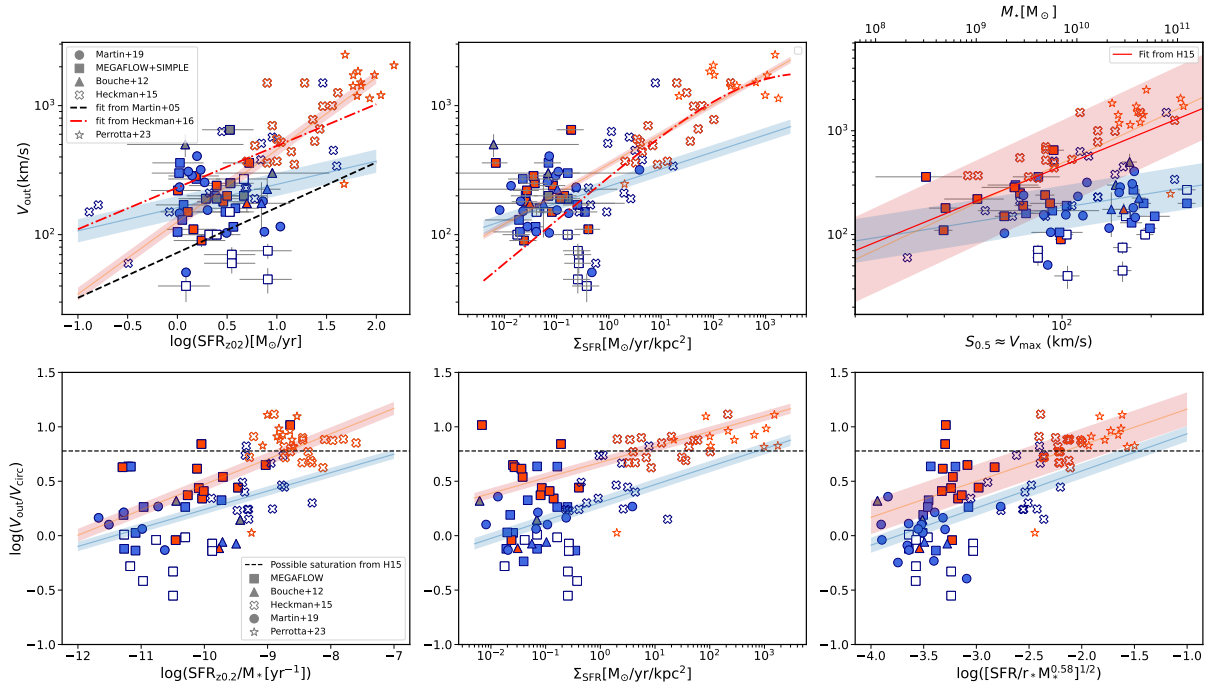


Fig. 3. Outflow velocity as a function of host galaxy properties. Top left: V_{out} as a function of SFR for MEGAFLOW and SIMPLE as well as observations from all the samples used in this study. The dashed black line shows a fit ($\log V = (0.35 \pm 0.06) \log(\text{SFR}) + (1.56 \pm 0.13)$) from [Martin \(2005\)](#). The errors on the [Heckman et al. \(2015\)](#) observations are 0.2 dex for SFR and 0.05 dex for V_{out} . Top middle: V_{out} as a function of Σ_{SFR} for the same surveys as in the left panel. Top right: V_{out} as a function of $S_{0.5}$. The red dot-dashed line shows a fit from H16. In these three panels, red (blue) observations correspond to starbursts (SFGs) for P23 or strong (weak) outflows for MEGAFLOW, M19, and H15. Bottom: outflow velocity normalized by the galaxy circular velocity as a function of the specific SFR (SFR/M_*), SFR surface density (Σ_{SFR}), and a combination of specific SFR and Σ_{SFR} found in H15 (from left to right).

3.3. Wind scaling relations

Because galaxy properties like SFR and mass are thought to be directly linked with properties of galactic winds (e.g., [Heckman et al. 2000, 2015](#); [Martin 2005](#); [Hopkins et al. 2012](#); [Newman et al. 2012](#)), we investigate the relations, if any, between outflow properties like their velocity V_{out} , their ejected mass rate \dot{M}_{out} , and their loading factor η with these main galaxy properties.

3.3.1. Scaling relations involving V_{out}

To estimate V_{out} , one does not necessarily need a background quasar. Many other studies derived outflow velocities with high enough accuracy (± 10 – 20% ; e.g., [Martin 2005](#); [Genzel et al. 2011](#); [Newman et al. 2012](#); [Arribas et al. 2014](#); [Heckman et al. 2015](#)). These studies found a significant, but scattered, correlation between the outflow velocity and galaxy SFRs at low redshift ([Heckman et al. 2000, 2015](#); [Martin 2005](#); [Rupke et al. 2005](#); [Martin et al. 2012](#); [Arribas et al. 2014](#)). [Martin \(2005\)](#) derived an upper limit on V_{out} as a function of SFR. This limit corresponds to the upper envelope of the outflow velocity distribution at a given SFR.

We show in [Appendix A](#) that down-the-barrel and background quasar derived outflow velocities give similar outflow speeds V_{out} , and are therefore comparable. It is also worth mentioning that background quasar measurements are made at larger radii than down-the-barrel measurements, and hence suffer from time travel effects that could obscure correlations with SFR if the SFR varies in time. This effect is discussed in [papers II and III](#) and is one of the reasons why only galaxy-quasar pairs that have

impact parameters ≤ 100 kpc were selected in these studies. This reduces the possible effect of the time traveling effect on SFR estimation, but does not remove it completely.

In [Fig. 3](#) we investigate the dependence of V_{out} on SFR, SFR surface density, Σ_{SFR} , and V_{circ} , in the top left, middle, and right panels, respectively. In the left panel, we corrected the SFRs for the redshift evolution of the MS using [Boogaard et al. \(2018\)](#) in order to have all SFRs at the same redshift ($z = 0.2$ in this case to match H15). The dashed black line represents the upper outflow velocity found by [Martin \(2005\)](#) for a small sample of local galaxies. They found that V_{out} increases with SFR, and their upper limit seems to underestimate V_{out} for a given SFR.

The red dot-dashed line in the top left and middle panels represents the positive correlation found by H15 and [Heckman & Borthakur \(2016\)](#). The red (blue) line with the shaded area represents our power law fit, which uses a least squares fitting method, of the strong (weak) population, and its error obtained using the bootstrap method on 100k realizations. We find that the correlation between V_{out} and the reduced SFR is positive for the strong outflows ($V_{\text{out}} \propto \text{SFR}^{0.6 \pm 0.07}$). For the weak outflows in blue, a weaker correlation can be seen ($V_{\text{out}} \propto \text{SFR}^{0.2 \pm 0.09}$). The bootstrap fitting results are given in [Table 2](#).

There have been disagreements about the existence of a correlation between V_{out} and SFR surface density (Σ_{SFR}) (e.g., [Chen et al. 2010](#); [Rubin et al. 2014](#); [Genzel et al. 2011](#); [Newman et al. 2012](#)). In the top middle panel of [Fig. 3](#), we show the outflow velocity V_{out} as a function of Σ_{SFR} ⁸.

⁸ Since Σ_{SFR} is correlated by the galaxy size, which is correlated with M_* , we thus do not normalize for redshift evolution for this quantity.

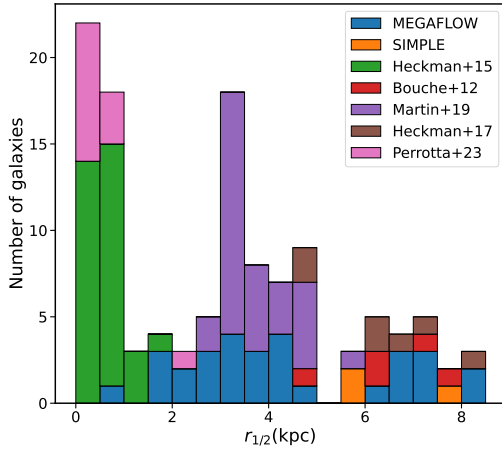


Fig. 4. Distributions of half-light radius $r_{1/2}$ for all the samples: MEGAFLOW, SIMPLE, H15, Bouché et al. (2012), M19, Heckman et al. (2017), and P23 in blue, orange, green, red, purple, maroon, and pink, respectively.

Heckman & Borthakur (2016) found a strong correlation between these two quantities. Adding our observations as well as M19 to their sample confirms this correlation.

We also point out that the H15 Σ_{SFR} are large compared to those of MEGAFLOW galaxies. Figure 1 shows that the H15 galaxies have higher SFRs than the MEGAFLOW galaxies. To check whether the large Σ_{SFR} values of H15 were due to only SFRs or also sizes, Fig. 4 shows the distribution of half-light radius of samples used in this study. We see that the H15 galaxies tend to be much smaller. This contributes to the fact that their Σ_{SFR} values are quite large compared to MEGAFLOW or M19 galaxies. Using the same bootstrap method as for the top left panel of this figure, there is no large difference between strong and weak outflows, $V_{\text{out}} \propto \Sigma_{\text{SFR}}^{0.2 \pm 0.03}$ and $V_{\text{out}} \propto \Sigma_{\text{SFR}}^{0.1 \pm 0.05}$, respectively.

The next step is to investigate whether the outflow velocity depends on the host galaxy mass. Following the SFR- M_{\star} relation (Fig. 1) and the tendency of V_{out} to increase with the host galaxy star formation rate, we could expect the outflow velocity to also correlate with the host galaxy mass. However, a more massive galaxy has a deeper gravitational well, and thus it is more difficult for the gas to accelerate. The top right panel of Fig. 3 shows the relation between V_{out} and $S_{0.5}$.

For the weak outflows from MEGAFLOW and M19 (in blue), outflow velocities are almost constant at around 100–200 km s⁻¹, while for the strong outflows (red points) V_{out} indeed strongly correlates with galaxy mass, which confirms the results from H15, represented by the red curve in the top right panel. Using the bootstrap fitting method, we indeed find that strong outflows have a steeper slope with $S_{0.5}$ ($V_{\text{out}} \propto S_{0.5}^{1.3 \pm 0.2}$) than in the case for weak outflows ($V_{\text{out}} \propto S_{0.5}^{0.5 \pm 0.21}$).

To summarize, V_{out} correlates with SFR and with Σ_{SFR} . V_{out} also correlates with the host galaxy mass if outflows are strong and is weakly mass-dependent for weak outflows. In other words, we begin to see a difference in outflow properties between weak and strong outflows where strong outflows appear to correlate more strongly with galaxy properties than weak ones. Distinguishing between those two outflow populations allows us to confirm that the formalism of H15 is relevant to SFGs and starbursts.

In order to investigate further the possible scaling relations for the outflow velocity, in the bottom row of Fig. 3 we show V_{out} normalized by the galaxy circular velocity V_{circ} as a function

Table 2. Summary of bootstrap fitting.

Parameters (1)	Strong (2)	Weak (3)	Both (4)
$\log(V_{\text{out}})$			
$\log(\text{SFR}_{z=0.2})$	0.56 ± 0.05	0.18 ± 0.09	0.46 ± 0.05
$\log(\Sigma_{\text{SFR}})$	0.23 ± 0.03	0.13 ± 0.05	0.23 ± 0.02
$\log(S_{0.5})$	1.33 ± 0.20	0.45 ± 0.21	0.77 ± 0.18
$\log(\dot{M}_{\text{out}})$			
$\log(\text{SFR}_{z=0.2})$	0.47 ± 0.09	0.29 ± 0.17	0.40 ± 0.08
$\log(\Sigma_{\text{SFR}})$	0.16 ± 0.04	0.13 ± 0.11	0.17 ± 0.04
$\log(S_{0.5})$	1.27 ± 0.21	0.89 ± 0.41	1.09 ± 0.21
$\log(\eta)$			
$\log(\text{SFR}_{z=0.2})$	-0.57 ± 0.24	-0.35 ± 0.24	-0.43 ± 0.13
$\log(\Sigma_{\text{SFR}})$	-0.18 ± 0.04	-0.21 ± 0.10	-0.19 ± 0.04
$\log(S_{0.5})$	-1.01 ± 0.24	-0.99 ± 0.43	-0.89 ± 0.25

Notes. (1) Wind parameters: outflow velocity V_{out} , ejected mass rate \dot{M}_{out} , and mass loading factor η as a function of (if any correlation) $\text{SFR}_{z=0.2}$, Σ_{SFR} , and $S_{0.5}$; (2) strong outflow population; (3) weak outflow population; (4) both populations altogether.

of specific SFR corrected to $z = 0.2$ (bottom left panel), SFR surface density (Σ_{SFR}) (bottom middle panel), and a combination of specific SFR and Σ_{SFR} (bottom right panel).

One sees that the relative outflow speed $V_{\text{out}}/V_{\text{circ}}$ is a simple function (perhaps universal) of SFR, or of momentum injection rate (bottom left), and that, as mentioned in H15, there is a possible saturation in normalized outflow velocity when $V_{\text{out}} \approx 4V_{\text{circ}}$ above $\Sigma_{\text{SFR}} \sim 10 M_{\odot} \text{ yr}^{-1} \text{ kpc}^{-2}$. This saturation is shown with the horizontal black dashed line in each panel of the bottom row in Fig. 3. We can see that this saturation seems to be the case if we only look at H15 data. However, with the addition of the lower SFR data (MEGAFLOW + M19), this is no longer as convincing. In the bottom panels we also show the bootstrap fits for each outflow population in red and blue lines for strong and weak, respectively. Apart from the normalization of each fit, strong and weak outflows appear to correlate similarly with each quantity. These correlations are less scattered than with SFR, Σ_{SFR} , or M_{\star} , which we can directly compare with the top row, and there is no clear differentiation between the two outflow populations if we consider them together or independently (as shown by the corresponding correlation coefficients in Table 2).

3.3.2. Scaling relations for \dot{M}_{out}

We now turn to another fundamental wind property, namely the ejected mass outflow rate \dot{M}_{out} (and the mass loading factor $\eta \equiv \dot{M}_{\text{out}}/\text{SFR}$), and investigate possible scaling relations with the properties of the host galaxies. In order to compare the outflow ejection rates \dot{M}_{out} in Paper III to those in H15, where the mass ejection rate was estimated assuming spherically symmetric outflows with $\theta_{\text{max}} = 4\pi \text{sr}$, we scaled their \dot{M}_{out} to 60° using, as previously, V_{out} from Heckman & Borthakur (2016).

For the M19 galaxies, to estimate the mass ejection rate we used the Mg II REW as a proxy to estimate the N_{H} column density (Ménard & Chelouche 2009; Zhu & Ménard 2013). This proxy is only viable for strong Mg II REW, and we thus only selected the galaxies with $W_r^{\lambda 2796} > 0.5 \text{ \AA}$.

As in Fig. 3, the top panel of Fig. 5 shows the mass ejection rate (\dot{M}_{out}) as a function of SFR corrected to $z = 0.2$ (left panel), Σ_{SFR} (middle panel), and the galaxy mass (right panel). Regarding the \dot{M}_{out} -SFR relation, Hopkins et al. (2012)

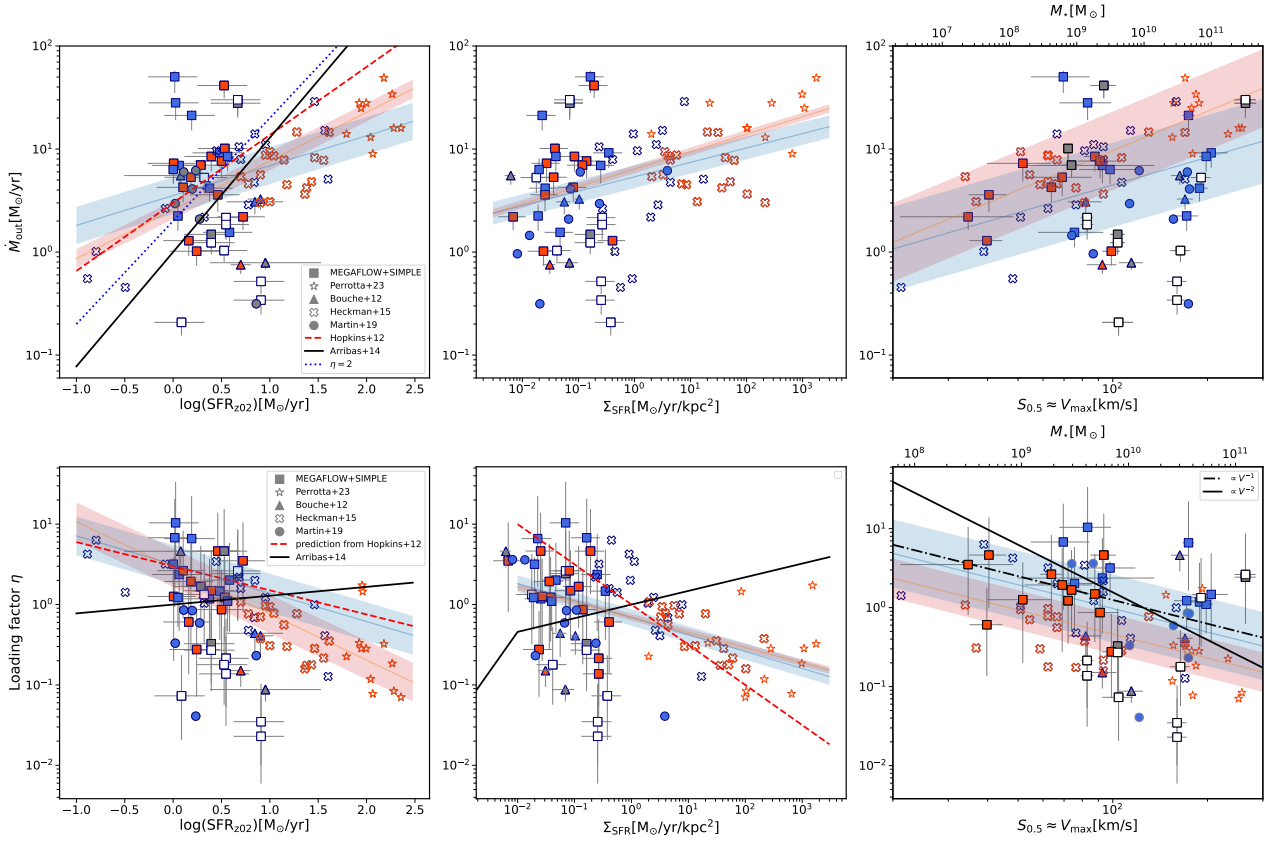


Fig. 5. Mass ejection rate and loading factor as a function of galaxy properties. Top: mass ejection rate as a function of star formation rate (left), star formation rate surface density (Σ_{SFR} , middle), and galaxy circular velocity (right, and stellar mass on top x-axis) for both surveys (MEGAFLOW and SIMPLE) as well as observations from B12, H15, M19, and P23. In the left panel, the dashed red line shows the prediction $\dot{M}_{\text{out}} \propto \text{SFR}^{0.7}$ from Hopkins et al. (2012) and the black line shows $\dot{M}_{\text{out}} \propto \text{SFR}^{1.11}$ observed by Arribas et al. (2014). The blue dotted line corresponds to a constant mass loading factor $\dot{M}_{\text{out}}/\text{SFR}$ of 2. Errors for Heckman et al. (2015) are 0.25 dex for \dot{M}_{out} and 0.2 dex for SFR and Σ_{SFR} . Bottom: η as a function of SFR (left), Σ_{SFR} (middle), and $S_{0.5}$ (right) for both surveys (MEGAFLOW and SIMPLE) as well as observations from B12, H15, M19, and P23. In the left panel, the dashed red line shows the prediction $\eta \propto \text{SFR}^{-0.3}$ from Hopkins et al. (2012) and the black line shows the fit $\eta \propto \text{SFR}^{0.11}$ from Arribas et al. (2014). In the middle panel, the dashed red line shows the prediction $\eta \propto \Sigma_{\text{SFR}}^{-1/2}$ from Hopkins et al. (2012) and the black line shows the fit $\eta \propto \Sigma_{\text{SFR}}^{0.17}$ from Arribas et al. (2014). Again, errors for Heckman et al. (2015) are 0.2 dex for SFR (and Σ_{SFR}) and 0.45 dex for η . In the right panel, the dashed dotted black line shows $\eta \propto V^{-1}$ and the solid black line shows $\eta \propto V^{-2}$.

predicted that $\dot{M}_{\text{out}} \propto \text{SFR}^{0.7}$ (shown as the dashed red line in the left panel), whereas Arribas et al. (2014) observed a steeper index $\dot{M}_{\text{out}} \propto \text{SFR}^{1.11}$ (shown as a solid black line).

The amount of ejected mass by supernova explosions is directly linked to SFR, which means that it is intuitively expected that SFR correlates with \dot{M}_{out} . Looking by eye only at weak outflows, there is no obvious correlation, but for strong outflows the correlation between the mass ejection rate and the galaxy SFR appears to be in closer agreement with the Hopkins et al. (2012) predictions than with the observations of Arribas et al. (2014). For V_{out} we use the bootstrap fitting method to measure the relations between \dot{M}_{out} and the galaxy properties. In the top left panel of Fig. 5, both strong and weak outflows correlate slightly with SFR and the bootstrap slopes are close to each other, with the strong outflows having a steeper slope than the weak, $\dot{M}_{\text{out}} \propto \text{SFR}^{0.5 \pm 0.1}$ and $\propto \text{SFR}^{0.3 \pm 0.2}$ for the strong and weak populations, respectively.

Contrary to the correlation between V_{out} and Σ_{SFR} , the top middle panel of Fig. 5 shows that there is no correlation between the mass outflow rate and Σ_{SFR} , except perhaps a mild relation, which is confirmed by the bootstrap fitting as $\dot{M}_{\text{out}} \propto \Sigma_{\text{SFR}}^{0.16 \pm 0.04}$ for strong and $\propto \Sigma_{\text{SFR}}^{0.13 \pm 0.1}$ for weak outflows. Similarly, the top right panel of Fig. 5 indicates a weak correlation between

the ejected mass rate and $S_{0.5}$ (and thus its stellar mass) for both strong and weak outflows, albeit also with a large scatter ($\dot{M}_{\text{out}} \propto S_{0.5}^{0.8 \pm 0.4}$ for the weak populations and $\dot{M}_{\text{out}} \propto S_{0.5}^{1.3 \pm 0.2}$ for the strong ones).

3.3.3. Scaling relations for η

The last but perhaps the most important parameter concerning galactic outflows is the mass loading factor η (i.e., the ratio of the mass ejection rate \dot{M}_{out} to the SFR of the galaxy):

$$\eta = \frac{\dot{M}_{\text{out}}}{\text{SFR}} \propto \text{SFR}^{\alpha-1} \quad (8)$$

if $\dot{M}_{\text{out}} \propto \text{SFR}^{\alpha}$.

Depending on the value of α in Eq. (8), we can differentiate three cases: the correlation between η and SFR is positive ($\alpha > 1$), negative ($\alpha < 1$), or η can be constant ($\alpha = 1$). These three possibilities are represented by the lines in top left panel of Fig. 5 with $\alpha = 0.7$ (Hopkins et al. 2012), $\alpha = 1.11$ (Arribas et al. 2014), and $\alpha = 1$ (a constant loading factor $\eta = 2$), none of which actually fit the data. If a correlation exists, it has a lower α than Hopkins et al. (2012). According to the result of the bootstrap method in Table 2, α is around 0.4 regardless of outflow strength.

Thus, we can argue that if η correlates with SFR, it should be an anti-correlation ($\alpha < 1$). The bottom left panel of Fig. 5 shows the mass loading factor as a function of SFR. We can see a scattered anti-correlation between these two properties. This confirms that $\eta \propto \text{SFR}^{\alpha-1}$ with $\alpha < 1$. Our observations are thus in qualitative agreement with the Hopkins et al. (2012) predictions.

As there is no significant difference between weak and strong outflows, we can conclude that the mass loading factor indeed anti-correlates with the galaxy SFR regardless of the galaxy type. Thus, galaxies with high SFR tend to have a lower mass loading factor than galaxies with a lower SFR. We return to the implications of this result in Sect. 4.

As before, we investigate whether the mass loading factor depends on local galaxy properties (such as Σ_{SFR}) or global (such as mass). In the bottom middle panel of Fig. 5, we show η as a function of Σ_{SFR} . Prediction and observations from Hopkins et al. (2012) and Arribas et al. (2014) are represented by red dashed lines and black solid lines, respectively. It appears that there is a clear anti-correlation between η and Σ_{SFR} in the data. The slope of this anti-correlation seems to be the same for strong and weak outflows and the bootstrap fitting gives us the same slope for both populations (≈ -0.2).

It is worth mentioning that Arribas et al. (2014) and Newman et al. (2012) found that low- z galaxies and high- z galaxies, respectively, require a Σ_{SFR} larger than $1 M_{\odot} \text{ yr}^{-1} \text{ kpc}^{-2}$ for launching strong outflows. This statement is not supported by the MEGAFLOW or the M19 galaxies since the majority of them show outflow signatures and have Σ_{SFR} below $1 M_{\odot} \text{ yr}^{-1} \text{ kpc}^{-2}$, even if we only focus on the strong outflows. As seen in bottom right panel of Fig. 5, the mass loading factor anti-correlates with the galaxy stellar mass. We discuss the implications with regard to the correlation slopes in the next section.

Another aspect about the mass loading factor is its redshift dependence. As there is a peak in star formation density at redshift 2–3 (e.g., Lilly et al. 1996; Madau et al. 1996; Behroozi et al. 2013), if η correlates with SFR, one can expect a correlation between η and redshift. We thus investigated this relation, but found no evident correlation (as compared to Muratov et al. 2015). Figure B.1 in the shows η as a function of redshift for individual cases of each study and shows no apparent correlation. Finally, we find no correlation between η and V_{out} , in agreement with results from H15.

4. The mechanisms that drive galactic winds

We now use the results shown in the previous section to tackle the question of what mechanisms drive galactic winds out of the galactic disk. To date, two major mechanisms have been identified that could be responsible for driving materials out of the galaxy: energy-driven outflows and momentum-driven outflows (as reviewed in Heckman et al. 2017). The momentum-driven wind scenario considers that the two primary sources of momentum deposition in driving galactic winds are supernovae and radiation pressure from the central starburst. This model assumes that $\dot{M}_{\text{out}} V_{\text{out}}$ is constant and implies that η must be inversely proportional to V_{circ} (i.e., $\eta \propto V_{\text{circ}}^{-1}$), given that V_{out} scales as $S_{0.5}$, and thus as the galaxy circular velocity (e.g., Martin 2005; Oppenheimer & Davé 2006, 2008; Davé et al. 2011; Heckman et al. 2017).

The energy-driven wind model assumes that when stars evolve, they deposit energy into the ISM. The amount of gas blown out of the disk is assumed to be proportional to the total energy released by supernovae and inversely proportional to the escape velocity squared. In the energy-driven scenario, energy conservation implies $\eta \propto V_{\text{circ}}^{-2}$ (e.g., van den Bosch 2002).

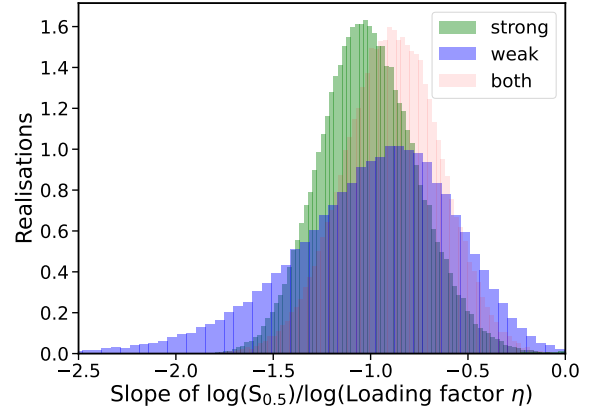


Fig. 6. Histogram of fitted slopes for 100k bootstrap normalized realizations of weak outflows (blue), strong outflows (green), and the combined samples (red).

In the bottom right panel of Fig. 5, we show the mass loading factor η as a function of galaxy $S_{0.5}$ (bottom x -axis) and galaxy stellar mass (top x -axis). In addition, we also show $\eta \propto V^{-2}$ (black line in the bottom right panel) in order to see if we could discriminate between the two mechanisms for driving outflows.

If we do not distinguish between weak and strong outflows, we find a scatter anti-correlation between η and $S_{0.5}$ with a slope of $\approx -0.9 \pm 0.3$. This slope value does not allow us to differentiate between momentum and energy-driven scenarios, but points toward a momentum-driven scenario nonetheless. Looking at strong and weak outflow populations individually, we find that the η anti-correlation with the galaxy stellar mass is steeper. We applied the bootstrap method to create 100k realizations of the weak and strong groups with 39 and 43 data points, respectively, as well as for the combined data; the resulting histogram of the fitted slopes of the loading factor $\eta - S_{0.5}$ relation is shown in Fig. 6. We can see that using all the data points, the mass loading factor $\eta \propto V^{-0.89 \pm 0.25}$, whereas for each population independently, we find $\eta \propto V^{-0.99 \pm 0.43}$ and $\eta \propto V^{-1.01 \pm 0.24}$ for weak and strong outflows, respectively. This slope is consistent with the prediction of Hopkins et al. (2012) ($\eta \propto S_{0.5}^{-1.2 \pm 0.2}$) and favors a momentum-driven scenario for galactic outflows.

5. Summary and conclusions

In this paper we used the results published in Paper III on outflow properties inferred from quasar absorption lines and compared them with other studies reporting mass ejection rates in order to investigate possible scaling relations between outflows and their host galaxy properties. The three main parameters we investigated are the outflow velocity V_{out} , the mass ejection rate \dot{M}_{out} , and the mass loading factor η . Those parameters were related to global galaxy properties, for example SFR, stellar mass, and SFR surface density.

We distinguished between two outflow regimes: weak and strong outflows (see Sect. 2.2). These regimes are the two cases where their momentum flux is higher or lower than ten times the critical momentum flux required to have a net outward force on an outflowing cloud (i.e., weak if $\log(\dot{p}_*/\dot{p}_{\text{crit}}) < 1.0$ and strong if $\log(\dot{p}_*/\dot{p}_{\text{crit}}) > 1.0$). For each parameter combination we used a bootstrap method in order to estimate the power law slopes of the relations between these properties. The two

⁹ We chose $S_{0.5}$ as we used this parameter to derive galaxy stellar masses. It is more appropriate to use this factor than the maximum rotation velocity as some of our galaxies are dispersion-dominated.

regimes show different behaviors, which can be summarize as follows:

- The outflow velocity correlates with SFR, Σ_{SFR} , and $S_{0.5}$ and shows stronger correlations for the strong outflow population. In particular, V_{out} exceeds the upper limit of Martin (2005) concerning its correlation with SFR.
- The mass ejection rate \dot{M}_{out} correlates, as the outflow velocity, with the three galaxy properties for both populations, but the strong outflows does not clearly correlate with SFR surface density.
- The mass loading factor anti-correlates with SFR, Σ_{SFR} , and $S_{0.5}$ for both populations. However, η is apparently not redshift dependent. The details of the different slopes are summarized in Table 2.
- We also find that the galaxy does not need $\Sigma_{\text{SFR}} > 1 M_{\odot} \text{yr}^{-1} \text{kpc}^{-2}$ in order to be able to launch material out of the galactic disk.
- In addition, we addressed the question of which mechanism is dominant and/or responsible for launching outflows. According to the bottom right panel of Fig. 5, we find that both weak and strong outflows point toward a momentum-driven scenario as the coefficient found for both populations is close to $\eta \propto V^{-1}$ with $\eta \propto V^{-1.01 \pm 0.24}$ and $\eta \propto V^{-0.99 \pm 0.43}$. This result needs to be confirmed with additional and more accurate results, but it shows that the mechanism responsible for launching the gas tends to be the same for the strong and weak outflow regimes.

In conclusion, using a bootstrap method on all galaxies and for the two regimes individually, we find that one needs to differentiate between strong and weak outflows as the two regimes have different behaviors. This differentiation is thus important to understand the role of galactic outflows in galaxy formation and evolution. We compared outflow properties derived from quasar absorption line and down-the-barrel methods and showed that a universal formalism can be used for outflows regardless of the method used. We mentioned that the background quasar line method has larger impact parameter than down-the-barrel and can suffer from time travel effects that could obscure correlation with SFR if the SFR varies during the time needed for the gas to get from the galaxy to the quasar line of sight. As this effect is discussed in the previous papers (papers I and III), we did not develop this effect here, but are aware that it may have an effect on results implying SFRs. Some results on properties like mass loading factors or mass ejection rates have order of magnitude uncertainties and are more indicative than accurate, but allowed us to nonetheless draw some conclusions using a bootstrap fitting method. Using the MEGAFLOW results on outflow properties and differentiating between weak and strong outflows, we confirm scaling relations as well as open new paths in the understanding of galactic winds properties and thus the evolution and formation of galaxies. Accuracy is essential in order to obtain the correct answers to these scaling relations, especially concerning wind properties like the mass outflow rate and mass loading factor. The background source method would greatly benefit from an accurate estimation of the hydrogen column density to be able to estimate lower column densities that can be inferred from Mg II absorption. Therefore, future observations are still needed. The *James Webb* Space Telescope allows higher redshift outflow studies and will provide many more outflow cases.

Acknowledgements. We thank the referee for her/his helpful comments and suggestions which helped to greatly improve the paper. This work has been carried out thanks to the support of the Agence Nationale de la Recherche (ANR) grant 3DGasFlows (ANR-17-CE31-0017) as well as support from the Centre National d'Etudes Spatiales (CNES) through the APR program.

References

- Alam, S., Albareti, F. D., Allende Prieto, C., et al. 2015, *ApJS*, 219, 12
- Alexandroff, R. M., Heckman, T. M., Borthakur, S., Overzier, R., & Leitherer, C. 2015, *ApJ*, 810, 104
- Arribas, S., Colina, L., Bellocchi, E., Maiolino, R., & Villar-Martín, M. 2014, *A&A*, 568, A14
- Bacon, R., Bauer, S., Böhm, P., et al. 2006, *Messenger*, 124, 5
- Bacon, R., Accardo, M., Adjali, L., et al. 2010, *SPIE Conf. Ser.*, 7735, 8
- Bacon, R., Brinchmann, J., Richard, J., et al. 2015, *A&A*, 575, A75
- Behroozi, P. S., Wechsler, R. H., & Conroy, C. 2013, *ApJ*, 762, L31
- Bergeron, J., & Stasinska, G. 1986, *A&A*, 169, 1
- Boogaard, L. A., Brinchmann, J., Bouché, N., et al. 2018, *A&A*, 619, A27
- Bordoloi, R., Lilly, S. J., Knobel, C., et al. 2011, *ApJ*, 743, 10
- Bouché, N., Murphy, M. T., Péroux, C., et al. 2007, *ApJ*, 669, L5
- Bouché, N., Hohensee, W., Vargas, R., et al. 2012, *MNRAS*, 426, 801
- Chabrier, G. 2003, *PASP*, 115, 763
- Chen, Y., Tremonti, C. A., Heckman, T. M., et al. 2010, *AJ*, 140, 445
- Chen, H.-W., Zahedy, F. S., Boettcher, E., et al. 2020, *MNRAS*, 497, 498
- Davé, R., Finlator, K., & Oppenheimer, B. D. 2011, *MNRAS*, 416, 1354
- Dekel, A., & Silk, J. 1986, *ApJ*, 303, 39
- Dekker, H., D'Odorico, S., Kaufer, A., Delabre, B., & Kotzlowski, H. 2000, *Proc. SPIE*, 4008, 534
- Genzel, R., Newman, S., Jones, T., et al. 2011, *ApJ*, 733, 101
- Grimes, J. P., Heckman, T., Aloisi, A., et al. 2009, *ApJS*, 181, 272
- Heckman, T. M., & Borthakur, S. 2016, *ApJ*, 822, 1
- Heckman, T. M., Lehnert, M. D., Strickland, D. K., & Armus, L. 2000, *ApJS*, 129, 493
- Heckman, T. M., Alexandroff, R. M., Borthakur, S., Overzier, R., & Leitherer, C. 2015, *ApJ*, 809, 147
- Heckman, T., Borthakur, S., Wild, V., Schiminovich, D., & Bordoloi, R. 2017, *ApJ*, 846, 151
- Ho, S. H., Martin, C. L., Kacprzak, G. G., & Churchill, C. W. 2017, *ApJ*, 835, 267
- Hopkins, P. F., Quataert, E., & Murray, N. 2012, *MNRAS*, 421, 3522
- Kacprzak, G. G., Churchill, C. W., Evans, J. L., Murphy, M. T., & Steidel, C. C. 2011, *MNRAS*, 416, 3118
- Kacprzak, G. G., Martin, C. L., Bouché, N., et al. 2014, *ApJ*, 792, L12
- Lan, T.-W., & Fukugita, M. 2017, *ApJ*, 850, 156
- Lilly, S. J., Le Fevre, O., Hammer, F., & Crampton, D. 1996, *ApJ*, 460, L1
- Lofthouse, E. K., Fumagalli, M., Fossati, M., et al. 2020, *MNRAS*, 491, 2057
- Lundgren, B. F., Creech, S., Brammer, G., et al. 2021, *ApJ*, 913, 50
- Madau, P., Ferguson, H. C., Dickinson, M. E., et al. 1996, *MNRAS*, 283, 1388
- Martin, C. L. 2005, *ApJ*, 621, 227
- Martin, C. L., Shapley, A. E., Coil, A. L., et al. 2012, *ApJ*, 760, 127
- Martin, C. L., Ho, S. H., Kacprzak, G. G., & Churchill, C. W. 2019, *ApJ*, 878, 84
- Mary, D., Bacon, R., Conseil, S., Piqueras, L., & Schutz, A. 2020, *A&A*, 635, A194
- Ménard, B., & Chelouche, D. 2009, *MNRAS*, 393, 808
- Moster, B. P., Naab, T., & White, S. D. M. 2013, *MNRAS*, 428, 3121
- Muratov, A. L., Kereš, D., Faucher-Giguère, C.-A., et al. 2015, *MNRAS*, 454, 2691
- Murray, N., Quataert, E., & Thompson, T. A. 2005, *ApJ*, 618, 569
- Muzahid, S., Kacprzak, G. G., Churchill, C. W., et al. 2015, *ApJ*, 811, 132
- Muzahid, S., Schaye, J., Marino, R. A., et al. 2020, *MNRAS*, 496, 1013
- Newman, S. F., Shapiro Griffin, K., Genzel, R., et al. 2012, *ApJ*, 752, 111
- Nielsen, N. M., Churchill, C. W., Kacprzak, G. G., & Murphy, M. T. 2013, *ApJ*, 776, 114
- Nielsen, N. M., Churchill, C. W., Kacprzak, G. G., Murphy, M. T., & Evans, J. L. 2015, *ApJ*, 812, 83
- Oppenheimer, B. D., & Davé, R. 2006, *MNRAS*, 373, 1265
- Oppenheimer, B. D., & Davé, R. 2008, *MNRAS*, 387, 577
- Perrotta, S., Coil, A. L., Rupke, D. S. N., et al. 2023, *ApJ*, 949, 9
- Rahmani, H., Péroux, C., Schroetter, I., et al. 2018, *MNRAS*, 480, 5046
- Ross, N. P., Myers, A. D., Sheldon, E. S., et al. 2012, *ApJS*, 199, 3
- Rubin, K. H. R., Prochaska, J. X., Koo, D. C., et al. 2014, *ApJ*, 794, 156
- Rupke, D. S., Veilleux, S., & Sanders, D. B. 2005, *ApJS*, 160, 115
- Schroetter, I., Bouché, N., Péroux, C., et al. 2015, *ApJ*, 804, 83
- Schroetter, I., Bouché, N., Wendt, M., et al. 2016, *ApJ*, 833, 39
- Schroetter, I., Bouché, N. F., Zabl, J., et al. 2019, *MNRAS*, 490, 4368
- Silk, J., & Rees, M. J. 1998, *A&A*, 331, L1
- Steidel, C. C., Bowen, D. V., Blades, J. C., & Dickinson, M. 1995, *ApJ*, 440, L45
- Steidel, C. C., Rudie, G. C., Strom, A. L., et al. 2014, *ApJ*, 795, 165
- Turner, M. L., Schaye, J., Steidel, C. C., Rudie, G. C., & Strom, A. L. 2014, *MNRAS*, 445, 794
- van den Bosch, F. C. 2002, *MNRAS*, 331, 98
- Zabl, J., Bouché, N. F., Schroetter, I., et al. 2019, *MNRAS*, 485, 1961
- Zhu, G., & Ménard, B. 2013, *ApJ*, 770, 130

Appendix A: Measuring outflow speeds

To estimate the outflow velocity, there are differences between the background quasar method and galaxy absorption method (known as the down-the-barrel method). The main difference is the background object. For quasar sightlines, it is known that the probed gas is likely to be in the CGM, while for galaxies (down-the-barrel) the gas can be anywhere in the CGM or IGM toward the observer. A background quasar also gives the location of the absorbing gas, namely the impact parameter, whereas absorption in a galaxy spectrum does not provide such information and is usually assumed to be several kiloparsec from the host galaxy.

In addition to this difference, the outflow absorption profile is different. In H15 the observer looks directly at the galaxy. The outflowing gas ejected from this galaxy is moving toward the observer. Thus, this gas gives rise to blueshifted absorption in the galaxy spectrum. In order to see this blueshifted absorption, the host galaxy needs to have a low inclination (to be close to a face-on configuration). Using a background quasar, the outflow absorption can be either blue- or redshifted with respect to the host galaxy systemic redshift. In addition, host galaxies are selected to be not face-on. The host galaxies selected in Paper III needed to have an inclination $i \geq 35^\circ$ for low position angle uncertainties.

To assess these differences, and thus confirm that we obtain similar results for the outflow velocity using our wind model, we first needed to create a configuration similar to the H15 method, namely a down-the-barrel configuration. We then created a wind model for this specific geometry. For a face-on galaxy, H15 used the outflow velocity value corresponding to 80–90% of the blueshifted absorption produced by the outflowing gas. This value will give the outflow velocity $V_{\text{out},90}$. This $V_{\text{out},90}$ was then corrected in Heckman & Borthakur (2016) to have the maximum outflow velocity of the gas. This maximum outflow velocity corresponds to our definition of V_{out} . We thus tried to see whether the V_{out} derived by H15 is similar to the value we derived from our wind model.

The aim was to see if we could reproduce the blueshifted absorption shape of their data seen in Fig. 1 of their paper, and also where V_{out} ends up. We created a wind model of a galaxy with an inclination of $i = 0^\circ$, azimuthal angle of 90° , and an impact parameter b of 0 kpc.

This model is shown in Fig. A.1. The top left panel of this figure is a representation of the sky plane of the face-on galaxy with the outflowing cone directed toward the observer. The top right panel represents a side view of the system, showing the line of sight in orange crossing the outflowing cone from right to left. Since the line of sight crosses all the way from the galaxy to the outer part of the cone, we created an accelerated wind model (tracing the accelerating part of the outflow; this model is described in Schroetter et al. 2015). This accelerated wind model changes the asymmetry of the profile as there are more clouds with lower velocity close to the galaxy.

The bottom panel of Fig. A.1 shows the resulting absorption profile of this configuration. The red vertical dashed line represents the input V_{out} . We see that this outflowing velocity corresponds to the furthest part of the blueshifted absorption. This is in agreement with the V_{out} derived by H15, corrected in Heckman & Borthakur (2016). We can thus directly compare our

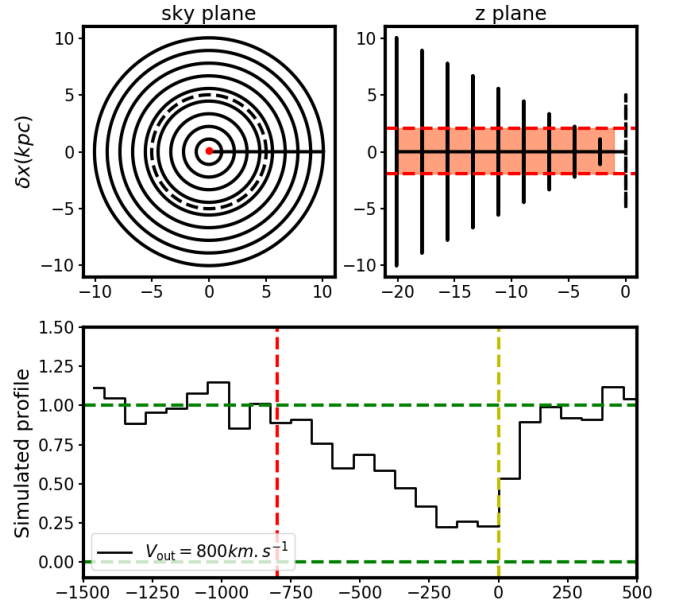


Fig. A.1. Wind model using a similar configuration to that used in H15. Top left: Sky plane representation of the system. The dashed black circle corresponds to the face-on galaxy. The black circles represent the outflowing cone and the red dot represents the center of the line of sight crossing the outflowing cone. Top right: Side view of the system. The galaxy is represented on the right as a dashed vertical line, the outflowing cone as the vertical black lines going to the left. The line of sight is represented by the red filled rectangle crossing the outflowing cone. Bottom: Resulting simulated absorption profile. The vertical red dashed line represents the outflow velocity used as input for this wind model. The simulated profile was convolved with the resolution used in H15 ($\sim 75 \text{ km s}^{-1}$ FWHM).

results with those of H15. Even if we did not include galaxies from Arribas et al. (2014) we still considered the relations they found to see if there are significant differences between SFGs and Ultra/Luminous infrared galaxies outflow properties.

Martin et al. (2019) used the background quasar method for the galaxies in their sample, and thus we can easily derive their outflow velocities. For their galaxies, we used the maximum velocity offsets (blue- or red-shifted) of the Mg II absorptions seen in background quasars as projected outflow velocities. Then, using the inclination derived in their study and a cone opening angle of 30° , we obtained the estimated outflow velocities V_{out} . From these outflow velocities, impact parameters, and W_r^{12796} , we estimated the mass outflow rates \dot{M}_{out} using Eq. (5) of Schroetter et al. (2015). Then, mass loading factors η were estimated using SFRs. Since their SFRs were derived using the M19 main sequence figure, we emphasize that their results are more indicative than accurate.

For the P23 outflow velocities, as for M19, we assumed the outflow velocity to be the maximum Mg II absorption velocity offsets. We note that they also have Fe II absorption velocities, but for consistency we chose to only use the Mg II values since we do the same for background quasars. P23 also already have ejected mass outflow rate for the bi-conical outflow geometry and for the corresponding loading factors, and we thus did not need to re-estimate them.

Appendix B: Mass loading factor redshift evolution

Figure B.1 shows the mass loading factor as a function of host galaxy redshift. As mentioned in the text, there is no apparent correlation between the mass loading factor and the host galaxy redshift.

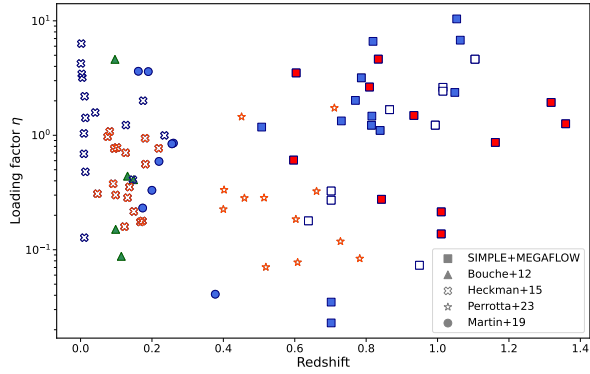


Fig. B.1. Mass loading factor as a function of host galaxy redshift. All points are individual results of both η and redshift from the studies mentioned in the legend.

Appendix C: Outflow velocity versus impact parameter

Figure C.1 shows the outflow velocity as a function of impact parameter for background source studies. As mentioned in the text, there is no apparent correlation between these parameters.

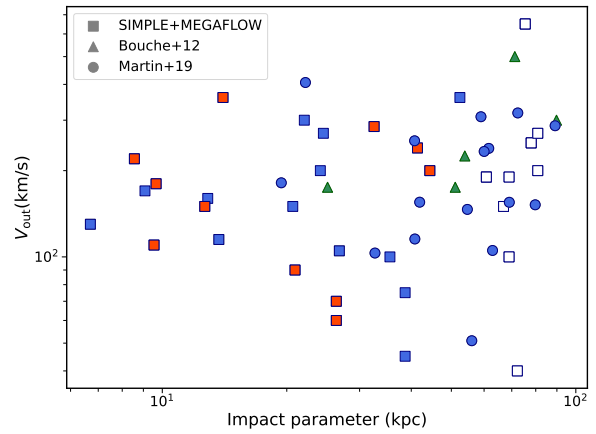


Fig. C.1. Outflow velocity as a function of the impact parameter for background sources studies.

Appendix D: Galaxy properties

The following tables list all the galaxy properties used in this paper in order to be able to reproduce the results.

Table D.1. Summary of galaxy properties.

Study (1)	V_{out} (2)	$\log(\text{SFR}_{0.2})$ (3)	Σ_{SFR} (4)	$S_{0.5}$ (5)	\dot{M}_{out} (6)	η (7)	\dot{p}_{\star} (8)	$\log(\dot{p}_{\text{crit,c}})$ (9)	$\log(\dot{p}_{\text{crit,s}})$ (10)
Paper III	180.0	0.461	0.0253	40.38	1.799	4.984	33.53	32.35	32.60
...	360.0	0.025	0.0698	83.16	14.04	10.39	34.11	33.75	33.85
...	200.0	0.376	0.0254	188.6	2.085	1.179	34.22	33.84	35.27
...	100.0	0.320	0.0177	190.8	2.642	1.334	34.27	34.22	35.29
...	150.0	0.482	0.3487	205.5	4.593	1.470	34.47	34.16	35.42
...	170.0	0.062	0.2500	92.67	3.464	2.367	34.14	33.26	34.04
...	70.0	0.546	0.2656	82.87	1.079	0.249	34.61	32.93	33.84
...	650.0	0.527	0.1906	93.61	20.69	4.620	34.63	33.50	34.06
...	160.0	0.583	0.0470	75.55	0.776	3.025	33.39	32.58	33.68
...	90.0	0.242	0.0237	98.98	0.509	0.275	34.24	32.85	34.15
...	250.0	0.533	0.0379	72.09	5.061	1.226	34.59	33.14	33.60
...	100.0	0.394	0.1627	103.6	0.617	0.270	34.33	33.85	34.23
...	45.0	0.908	0.2547	160.0	0.170	0.022	34.85	33.98	34.99
...	240.0	0.394	0.0848	87.68	4.236	1.489	34.43	33.37	33.94
...	270.0	0.191	0.0225	174.0	10.60	6.615	34.18	34.19	35.13
...	40.0	0.086	0.3769	104.3	0.103	0.073	34.13	33.60	34.24
...	220.0	0.005	0.0270	51.75	3.632	2.268	34.18	32.60	33.03
...	270.0	0.667	0.0698	264.1	15.04	2.623	34.74	34.80	35.86
...	300.0	0.016	0.1635	69.61	25.11	20.32	34.07	33.62	33.54
...	200.0	0.500	0.1397	91.09	3.819	0.866	34.62	33.53	34.01
...	150.0	0.527	0.0413	164.1	0.517	0.178	34.44	34.07	35.03
...	360.0	0.722	0.0068	34.69	1.100	7.013	33.17	31.78	32.33
...	150.0	0.103	0.0808	63.81	2.124	2.640	33.88	32.71	33.39
...	110.0	0.161	0.4056	39.78	0.645	1.138	33.73	32.01	32.57
...	190.0	0.286	0.1179	73.94	3.485	1.673	34.30	33.03	33.65
...	285.0	0.183	0.0360	69.06	2.660	2.582	33.99	32.96	33.53
...	190.0	0.394	0.1627	103.6	0.742	0.325	34.33	33.85	34.23
...	75.0	0.908	0.2547	160.0	0.259	0.034	34.85	33.98	34.99
...	200.0	0.667	0.0698	264.1	13.92	2.429	34.74	34.80	35.86
...	60.0	0.546	0.2656	82.87	0.925	0.214	34.61	32.93	33.84
H15	350	15.0	8.5113	83	33.0	0.300	34.9	33.4	33.9
...	530	24.0	36.307	108	26.0	0.175	35.1	33.4	34.3
...	450	37.0	3.1622	161	97.0	0.409	35.3	34.4	35.0
...	1500	19.0	19.952	184	39.0	0.769	35.0	33.9	35.3
...	1500	8.0	213.79	115	9.0	0.376	34.6	32.8	34.4
...	370	10.0	13.182	52	34.0	0.308	34.7	32.8	33.1
...	1500	29.0	7.7624	225	74.0	0.996	35.2	34.4	35.6
...	550	10.0	3.4673	72	48.0	0.942	34.7	33.4	33.6
...	520	11.0	3.9810	88	37.0	0.780	34.7	33.5	34.0
...	360	8.0	3.2359	77	30.0	0.703	34.6	33.4	33.7
...	990	29.0	41.686	151	30.0	0.284	35.1	33.7	34.9
...	510	7.0	0.9549	94	99.0	2.003	34.5	33.8	34.1
...	570	9.0	2.4547	123	45.0	1.228	34.6	33.9	34.6
...	370	5.0	2.0417	48	3.5	1.079	34.4	33.0	32.9
...	780	23.0	102.32	132	15.0	0.158	35.0	33.3	34.7
...	440	14.0	4.3651	94	47.0	0.559	34.8	33.6	34.1
...	660	27.0	51.286	88	21.0	0.178	35.1	33.2	34.7
...	490	6.0	6.9183	94	21.0	0.765	34.5	33.3	34.1
...	700	9.0	5.6234	88	35.0	0.972	34.6	33.4	34.0
...	1000	36.0	60.255	132	28.0	0.216	35.2	33.5	34.7
...	1260	41.0	30.902	240	46.0	0.353	35.3	34.2	35.7
...	150	0.83	0.2691	88	4.8	3.189	33.6	33.5	34.0
...	60	0.32	0.5623	30	2.3	1.418	33.2	32.2	32.1
...	230	5.0	0.4073	132	33.0	1.581	34.4	34.2	34.7

(1) Study; (2) Outflow velocity V_{out} (km s^{-1}); (3) $\text{SFR}_{z0.2}$ ($M_{\odot} \text{ yr}^{-1}$); (4) Σ_{SFR} ($M_{\odot} \text{ yr}^{-1} \text{ kpc}^{-2}$); (5) Galaxy maximum rotational velocity (or $S_{0.5}$) (km s^{-1}); (6) Ejected mass rate \dot{M}_{out} ($M_{\odot} \text{ yr}^{-1}$); (7) Mass loading factor η ; (8) Momentum injection rate; (9) Critical momentum flux; (10) Critical momentum flux for a shell model.

Table D.2. Summary of galaxy properties continued.

Study (1)	V_{out} (2)	$\log(\text{SFR}_{0.2})$ (3)	Σ_{SFR} (4)	$S_{0.5}$ (5)	\dot{M}_{out} (6)	η (7)	\dot{p}_{\star} (8)	$\log(\dot{p}_{\text{crit,c}})$ (9)	$\log(\dot{p}_{\text{crit,s}})$ (10)
H15	170	0.16	0.4466	55	1.0	6.324	32.9	32.7	33.2
...	190	6.0	2.6302	108	4.6	0.479	34.5	33.6	34.3
...	630	2.8	1.1220	115	22.0	3.437	34.1	33.7	34.4
...	340	40.0	16.982	240	12.0	0.127	35.3	34.3	35.7
...	150	0.13	0.9120	68	1.0	4.242	32.8	32.6	33.5
...	210	2.1	1.9498	72	5.4	1.038	34.0	33.1	33.6
...	230	4.8	0.2344	132	30.0	2.191	34.4	34.3	34.7
...	380	6.9	4.3651	151	4.6	0.688	34.5	33.9	34.9
B12	175.0	0.765	0.0308	92.63	0.376	0.150	34.38	33.30	35.00
...	500.0	0.147	0.0062	163.3	2.763	4.605	33.76	33.59	35.08
...	300.0	1.010	0.0690	114.5	0.394	0.087	34.63	32.89	34.90
...	175.0	0.889	0.0559	82.03	1.537	0.439	34.52	33.61	34.84
...	225.0	0.936	0.1035	169.7	1.635	0.408	34.58	33.73	35.21
M19	105.3	0.125	0.0408	91.54	0.005	0.008	32.81	31.07	34.02
...	181.38	0.149	0.0205	173.9	0.157	0.231	32.80	32.89	35.13
...	50.98	1.204	0.4732	89.42	0.001	0.000	33.75	30.87	33.98
...	286.93	0.712	0.0965	157.1	0.955	0.369	33.53	33.36	34.96
...	239.17	0.388	0.0134	74.10	0.725	3.601	...	32.68	33.65
...	308.43	0.809	0.1078	172.6	2.995	0.853	33.60	33.88	35.12
...	152.0	0.065	0.0228	117.6	0.169	0.384	...	32.63	34.45
...	155.09	0.508	0.1015	102.9	0.253	0.140	33.42	32.63	34.22
...	155.21	0.551	0.0081	86.66	0.481	3.624	...	32.85	33.92
...	317.98	2.074	3.8574	121.3	3.085	0.040	34.01	33.50	34.51
...	115.48	0.039	0.0276	144.1	0.012	0.020	32.71	31.74	34.81
...	254.21	0.535	0.0668	155.9	1.044	0.591	33.42	33.44	34.94
...	146.47	1.061	0.1706	176.7	0.061	0.010	33.70	32.55	35.16
...	406.11	0.652	0.0722	175.3	2.047	0.841	33.51	33.61	35.15
...	103.14	0.327	0.0724	63.86	0.025	0.025	33.16	31.48	33.39
...	233.36	0.951	0.2375	113.0	1.476	0.330	33.65	33.36	34.38
P23	1204	2.046	981	183.7	34	0.184	35.94	31.39	35.23
...	1426	1.847	281	188.1	28	0.282	35.67	32.38	35.27
...	2480	1.686	1519	192.6	156	1.733	35.63	33.27	35.31
...	1718	1.768	1074	178.0	25	0.284	35.62	31.93	35.17
...	2051	2.177	100	251.3	16	0.070	36.03	32.78	35.77
...	1842	1.815	85	147.5	132	1.450	35.64	33.00	34.85
...	247	1.675	2	232.4	14	0.225	35.47	32.95	35.64
...	1138	1.933	1755	169.9	49	0.324	35.86	32.13	35.09
...	1728	1.982	104	257.3	16	0.083	35.96	31.74	35.81
...	1514	1.843	652	179.4	9	0.077	35.74	31.25	35.19
...	1188	1.806	22	155.9	28	0.333	35.60	31.19	34.94
...	1421	1.765	216	154.6	13	0.118	35.72	32.58	34.93

(1) Study; (2) Outflow velocity V_{out} (km s^{-1}); (3) $\text{SFR}_{0.2}$ ($M_{\odot} \text{ yr}^{-1}$); (4) Σ_{SFR} ($M_{\odot} \text{ yr}^{-1} \text{ kpc}^{-2}$); (5) Galaxy maximum rotational velocity (or $S_{0.5}$) (km s^{-1}); (6) Ejected mass rate \dot{M}_{out} ($M_{\odot} \text{ yr}^{-1}$); (7) Mass loading factor η ; (8) Momentum injection rate; (9) Critical momentum flux; (10) Critical momentum flux for a shell model.